Title: Estimation of the velocity of a projectile using radial accelerometers - validation on 155mm free flight test

Authors: Aurélien Fiot[1,2]
Sébastien Changey[1]
Ronan Adam[1]
Nicolas Petit[2]

This paper addresses the problem of velocity estimation for a 155 mm projectile. Indeed, to correctly feed the guidance and control algorithms of such a guided munition, it is essential to estimate its speed autonomously (without any external system) onboard and in real-time. Knowledge of the velocity (and thus the Mach number) is required to infer the aerodynamic coefficients governing its dynamics. From the analysis of the frequencies present on one of the radial accelerometers, and from a reduced 6DOF model describing the epicyclic rotation of the shell, we are able to estimate the velocity of the ammunition. The roll speed can be determined from magnetometers. For frequency estimation, we employ a subspace method of the Pisarenko type, relying on the auto-correlation matrix of the accerelometer signal. This matrix is estimated from samples and its dominant eigenvalues are related to the precession and nutation frequencies. In turn, the velocity can be estimated from the analytical values of the epicyclic motion. In this paper, we offer an efficient method to estimate the velocity of an artillery shell in free-flight, using only embedded sensors. The next step will be to use these results to improve the estimation of the projectile's attitude and position.

INTRODUCTION

This paper addresses the problem of velocity estimation for a 155 mm projectile. Indeed, to correctly feed the guidance and control algorithms of such a guided munition, it is essential to estimate its speed autonomously (without any external system) onboard and in real-time. Knowledge of the velocity (and thus the Mach number) is required to infer the aerodynamic coefficients governing its dynamics.

[1]French-German Research Institute of Saint-Louis, ISL, Guidance, Navigation and Control Dept., 5 rue du Général Cassagnou, Saint-Louis, 68300, France
[2]MINES ParisTech, PSL University, CAS - Centre Automatique et Systèmes, 60 bd St Michel, Paris, 75272, France

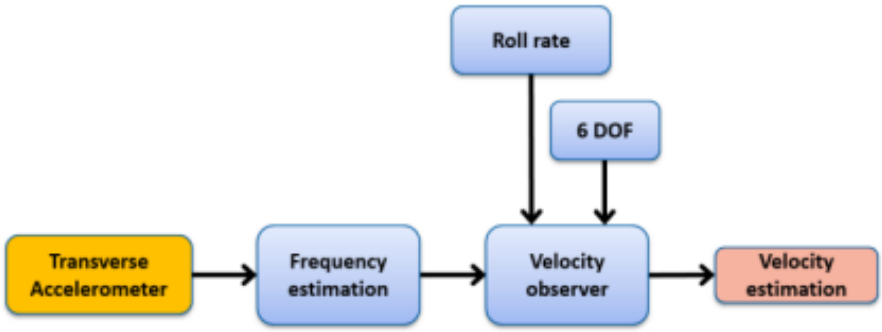

Figure 1: Estimation process.

From the analysis of the frequencies present on one of the radial accelerometers, and from a reduced 6DOF model describing the epicyclic rotation of the shell, we are able to estimate the velocity of the ammunition (see Figure 1). The roll speed can be determined from magnetometers.

For frequency estimation, we employ a subspace method of the Pisarenko type [26] [30], relying on the auto-correlation matrix of the accerelometer signal. This matrix is estimated from samples and its dominant eigenvalues are related to the precession and nutation frequencies. In turn, the velocity can be estimated from the analytical values of the epicyclic motion.

This paper focus on a specific part of the navigation methods developed in [12], on which we will briefly elaborate in the conclusion.

NOTATIONS AND PROBLEM STATEMENT

REFERENCE FRAMES AND SIX DEGREES OF FREEDOM DESCRIPTION

Let the frame L be defined by orthogonal unit vectors 1^L,2^L,3^L where 1^L direction is the direction of the shot on the horizontal plane and 3^L is vertical and pointing to the ground. This direct frame, referred to from now on as the "local frame", is an adaptation of the classical "North-East-Down" (NED) frame commonly used in aeronautics, rotated so that its first vector is oriented in the initial direction of the shot.

Classically, the shell can be modeled as a Six-Degrees-of-Freedom (6-DOF) rigid body. The full notations are summarized in Table I. The orientation of

Table I: Nomenclature.

x, y, z	Position of the shell in the local frame
v_x, v_y, v_z	Velocity of the shell w.r.t. the local frame
$h = -z > 0$	Altitude of the shell
V	Velocity of the shell w.r.t. the airflow
$v = \|V\|$	Scalar velocity of the shell w.r.t. the airflow
N_{mach}	Mach number of the shell
v_B^L	Velocity of the shell w.r.t. the local frame
X	Position of the shell w.r.t. the local frame
$R = [T]^{LB}$	Attitude matrix of the shell
	(transition matrix from the local frame to the body frame)
Ψ, Θ, Φ	Tait-Bryan angles
Ψ	Yaw angle
Θ	Pitch angle
Φ	Roll angle
$\Omega = (p, q, r)$	Angular velocity of the shell w.r.t. the local
	frame expressed in the body frame
ω_L^I	Angular velocity of the local frame w.r.t.
	a geocentric frame (Earth's rotation, adding Coriolis effect)
$p = \langle \Omega, 1^B \rangle$	Spin rate of the shell (or longitudinal component of Ω)
$q = \langle \Omega, 2^B \rangle$	transverse component of Ω along 2^B
$r = \langle \Omega, 3^B \rangle$	transverse component of Ω along 3^B
$[T]^{BW}$	Transition matrix from the body
	frame to the wind velocity frame
α, β	Incidence angles (see below)
α	Attack angle
β	Sideslip angle
α_t	Total angle of attack of the shell
	(angle between vectors 1^B and V)
θ	Slope angle
	("pitch" angle of $[T]^{LW}$ in "ZYX" decomposition)

the rigid body is defined by a set of three Tait-Bryan angles (here "ZYX" angles are chosen, following the nomenclature of [20], where, as commonly considered, the spin is defined as the rotation about its axis of least inertia). As a result,

the orientation of the body with respect to the local inertial frame is described by the Tait-Bryan angle sequence:

$$\text{yaw: } \Psi, \text{ pitch: } \Theta, \text{ roll: } \Phi$$

The shell state comprises 12 variables, namely the position, velocity, attitude (under the form of the three angles previously introduced) and angular velocity. It reads

$$X_{full} = \begin{pmatrix} x & y & z & v_x & v_y & v_z & \Psi & \Theta & \Phi & p & q & r \end{pmatrix}^T \tag{1}$$

This vector contains several groups of variables of interest. Let us define the following partial state variables : the position X, the velocity V (and its norm $v = |V|$), three angles defining the attitude matrix R (and the corresponding quaternion q) and the angular velocity ω. Details are given in (2).

We note (e_1, e_2, e_3) a canonical base of $\mathbb{R}^3$, $R_{a,v}$ the matrix defining the 3D-rotation of angle a about the vector v, and $q_{a,v}$ one of the two unit quaternions representing $R_{a,v}$. Conversely, the $R_{a,v}$ matrix can be derived from the quaternion $q_{a,v}$.

$$\begin{cases} X = \begin{pmatrix} x & y & z \end{pmatrix}^T \\ V = \begin{pmatrix} v_x & v_y & v_z \end{pmatrix}^T \\ R = [T]^{LB} = R_{\Psi,e_3} R_{\Theta,e_2} R_{\Phi,e_1} \\ q = q_{\Psi,e_3} \otimes q_{\Theta,e_2} \otimes q_{\Phi,e_1} \\ \Omega = \begin{pmatrix} p & q & r \end{pmatrix}^T \end{cases} \tag{2}$$

Besides the local (inertial) frame L and the body B frame, a third frame is considered and referred to as the "wind velocity frame", denoted W. It is defined from the body frame using the velocity of the shell with respect to the airflow, denoted v_B^A or V, as described by Figure 2.

The attack angle α and the sideslip angle β are defined by

$$[T]^{BW} = R_{-\alpha,e_2} R_{\beta,e_3} \tag{3}$$

where $[T]^{BW}$ is the transition matrix from the body frame to the wind velocity frame

The angles between the frames L, B and W are illustrated in Figure 2.

ENVIRONMENT MODEL

The environment of the shell is modeled with standard atmosphere, gravity, and Earth magnetic field reference models. In details, following the Standard-

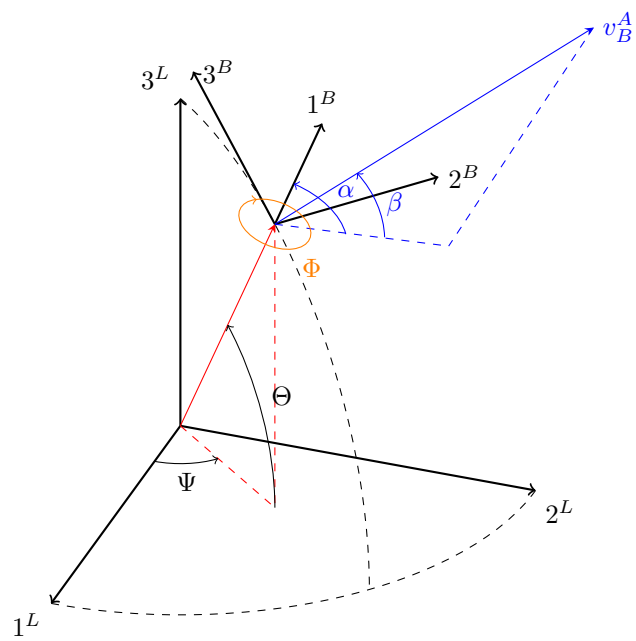

Figure 2: Definition of Tait-Bryan and incidence angles at $\Phi = 0$; α refers to a rotation around 2^B and β around 3^W.

ization Agreement STANAG 4355 from NATO, the gravitational acceleration at altitude h is

$$g(h) = g_0 \left(\frac{R}{R+h} \right)^2 \tag{4}$$

where

$$g_0 = 9\ 80665 \times (1 - 0\ 0026 \cos(2\,\mathrm{Lat}))$$

while R is an average value of the Earth radius and Lat is the geodetic latitude of the local frame L (g slightly increases when moving away from the equator).

At any altitude h, the air density is given, following [15],

$$\rho(h) = \rho_0 \left(\frac{T_0 - 0\ 0065h}{T_0} \right)^{4\ 2561} \tag{5}$$

with ρ_0 the air density on the ground. In turn, this defines the sound velocity

$$v_{\mathrm{sound}}(h) = a_0 \left(\frac{T_0 - 0\ 0065h}{T_0} \right)^{\frac{1}{2}} \tag{6}$$

where a_0 is the velocity of the sound at ground level. The Mach number is, as usual,

$$N_{\mathrm{mach}}(v, h) \triangleq \frac{v}{v_{\mathrm{sound}}(h)} \tag{7}$$

This variable is a main input of the aerodynamic forces and moment look-up tables introduced in Section .

The various constants appearing in the previous equations are given in Table II.

Table II: Environment constants.

Constant	value	unit
ρ_0	1 225	kg.m^{-3}
a_0	340 429	m.s^{-1}
R	$6\ 356766 \times 10^6$	m
Lat	45	deg
T_0	288 16	K

Throughout the thesis (in simulation and for the analysis of actual flight data), the values for the environment constants are those reported in Table II.

PROJECTILE MODEL: DIMENSIONAL PARAMETERS AND AERODYNAMIC COEFFICIENTS

In the thesis, we consider two types of projectiles : 155 mm shells, fired with a high spin rate thanks to a rifled barrel (granting gyroscopic stability), and Basic Finners, which are smaller and lighter, fired without any initial spin rate but possessing roll-inducing fins[3].

The 155 mm is an all-purpose standard for NATO armies. The Basic Finner is a more recent experimental shell which has served for many years as a reference projectile and was tested extensively in numerous aero-ballistic ranges and in wind tunnels. The model consists of a 20 deg nose cone on a cylindrical body with four rectangular fins. The main dimensional parameters of the projectiles are listed in Table III with typical values detailed in Table IV. Reliable look-up table for their aerodynamic coefficients have been established (see e.g. [31, 5, 10, 1]).

Table III: Dimensional parameters.

D	Caliber of the shell
S	Reference area of the shell
M	Mass of the shell
I_l	Longitudinal moment of inertia
I_t	Transverse moment of inertia
$\delta_{fin\,cant}$	Angle of the fins with the shell outer surface (for Basic Finner only)

Table IV: Type of projectiles studied.

Type	D (m)	S (m^2)	M (kg)	I_l ($kg.m^2$)	I_t ($kg.m^2$)
Basic Finner	0 028	$6\ 16 \times 10^{-4}$	0 4	$4\ 36 \times 10^{-5}$	$2\ 14 \times 10^{-3}$
155 mm	0 155	$1\ 89 \times 10^{-2}$	43 25	0 15	1 61

The coefficients defining the aerodynamics forces and moment are listed in Table V. Their values are reported as a function of the Mach number in Figure 3 for the 155 mm artillery shell and in Figure 4 for the Basic Finner, for a total angle of attack of zero degree. All the variables in Table V are functions of $(N_{\text{mach}}, \alpha_t)$.

[3]more precisely, a specific spin rate can be achieved by setting the initial velocity of the projectile and the angle $\delta_{fin\,cant}$ of its fins.

Table V: Aerodynamics coefficients. All the variables in Table V are functions of $(N_{\text{mach}}, \alpha_t)$.

C_D	Drag force coefficient
$C_{L\alpha}$	Lift force coefficient
C_{mag-f}	Magnus force coefficient
C_{mag-m}	Magnus moment coefficient
$C_{l\delta}$	Rolling moment coefficient
C_{spin}	Roll damping moment coefficient
C_{Mq}	Pitch damping moment coefficient
$C_{M\alpha}$	Overturning moment coefficient

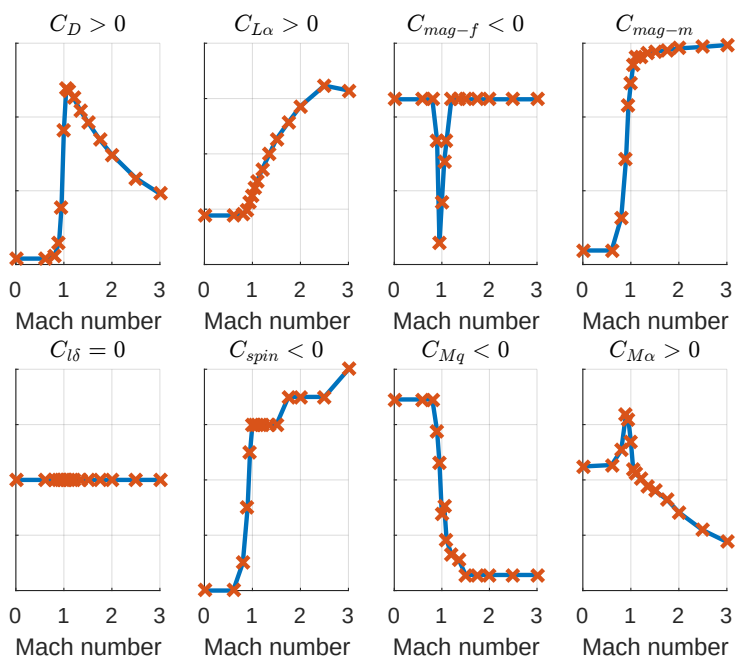

Figure 3: Aerodynamic coefficients profiles for 155 mm artillery shell.

FLIGHT DYNAMICS

For generality, the high velocity shell under consideration is a 6-DOF rigid body which is given both initial translational velocity and spin rate[4] by the gun launch. By contrast with rocket-propelled devices, the shell has a constant

[4]in the case of the Basic Finner, the initial spin rate can be simply set to zero.

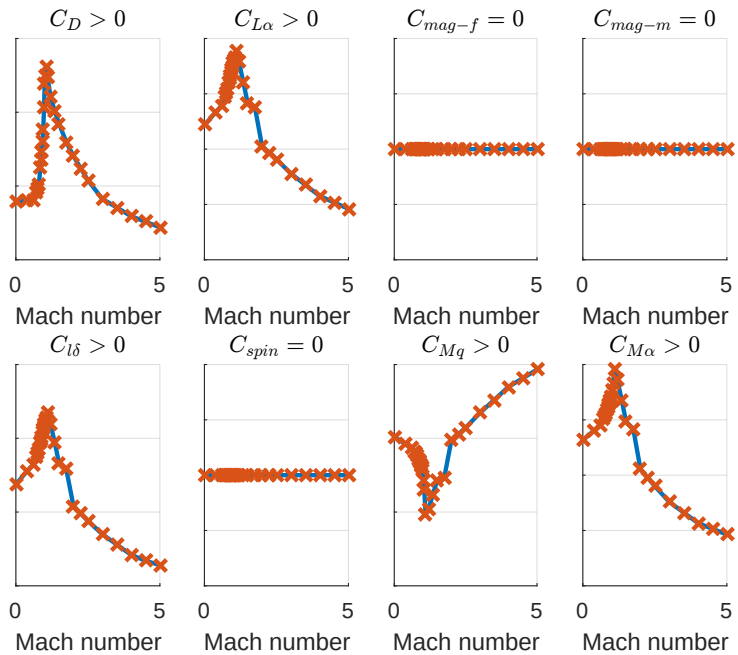

Figure 4: Aerodynamic coefficients profiles for Basic Finner.

mass during the whole flight. It is subjected to drag and lift forces, Magnus forces, Coriolis force, gravity, and several moments: Magnus, overturning [5], rolling [6], pitch damping and roll damping moments [24, 21]. These forces and moments have been extensively studied and measured using wind tunnels, free-flight ballistic ranges, spark and Schlieren photography among others methods. Experimentally established look-up tables are available for the two projectiles under consideration (see e.g. [31, 5]). Concise expressions are given in Table VI and Table VII, respectively.

TRANSLATIONAL DYNAMICS

After some reordering, the application of Newton Second Law yields, in a concise form

$$\dot{v} = -\frac{\rho S \tilde{C}_D v^2}{2M} - g \sin\theta, \quad \dot{h} = v \sin\theta \tag{8}$$

with

$$\tilde{C}_D(h, v, \alpha_t) \triangleq C_D(N_{mach}(h, v), \alpha_t) \tag{9}$$

[5] aerodynamic moment associated with the lift which is applied at the center of pressure.
[6] only for differentially canted finned shells, as the Basic Finner.

Table VI: Forces applied on the shell.

Force	Expression
Drag force	$-\frac{1}{2}\rho S C_D v v_B^A$
Lift force	$\frac{1}{2}\rho S C_{L\alpha}\left(v_B^A \times \left(1^B \times v_B^A\right)\right)$
Magnus force	$\frac{1}{2}\rho S\left(\frac{pD}{V}\right) C_{mag-f} v\left(v_B^A \times 1^B\right)$
Coriolis force	$2M v_B^L \times \omega_L^I$
Weight	Mg

Table VII: Moments applied on the shell.

Moment	Expression
Magnus moment	$\frac{1}{2}\rho S D\left(\frac{pD}{v}\right) C_{mag-m} v\left(1^B \times \left(v_B^A \times 1^B\right)\right)$
Overturning moment	$\frac{1}{2}\rho S D C_{M\alpha} v\left(v_B^A \times 1^B\right)$
Rolling moment	$\frac{1}{2}\rho S D \delta_{fin\,cant} C_{l\delta} v^2 1^B$
Pitch damping moment	$\frac{1}{2}\rho S D^2 C_{Mq} v\left(1^B \times \left(\Omega \times 1^B\right)\right)$
Roll damping moment	$\frac{1}{2}\rho S D\left(\frac{pD}{v}\right) C_{spin} v^2 1^B$

Equation (8) is obtained with some approximations, namely neglecting the difference between V the velocity of the shell w.r.t. the airflow and $\dot{X}$ the velocity in the local frame, and the contribution of the Coriolis force.

In (8), the drag is a dominant effect and deserves some more comments. Some effects of the shell shape on the drag coefficient at various Mach numbers have long been studied. Those effects depend on a number of dimensionless variables. The fluid mechanism that transmits the drag force to the shell consists of two parts: surface pressure and surface shear stress (a.k.a. skin friction drag). The force generated on the forebody and the base of the shell are different. Therefore, the various components of the drag force behave in significantly different ways in the various speed regions. At subsonic flight speeds (below Mach 1.0), the drag coefficient is essentially constant. It rises sharply near Mach 1.0, then slowly decrease at higher supersonic speeds. The sudden rise appearing just below Mach 1.0 is caused by the formation of shock waves in the flow-field surrounding the shell [24]. This rise is visible in the C_D profiles of Figure 3 and Figure 4.

ROTATIONAL DYNAMICS

Euler equation of rotation of a rigid body subjected to external aerodynamic moments can be written under the following form. One shall note the cancellation

of the bilinear term $q\,r$ in (10) due to the symmetric nature of the shell.

$$\dot{p} = \frac{\rho(h)SD^2C_{spin}v}{2I_l}p + \frac{1}{2}\rho(h)SD\delta_{fin\,cant}C_{l\delta}v^2 \tag{10}$$

$$\dot{q} = \frac{1}{I_t}\left((I_l - I_t)p\,r + \frac{1}{2}\rho SpD^2C_{mag-m}v\beta + \frac{1}{2}\rho SDC_{M\alpha}v^2\alpha + \frac{1}{2}\rho SD^2C_{Mq}vq\right) \tag{11}$$

$$\dot{r} = \frac{1}{I_t}\left((I_l - I_t)p\,q + \frac{1}{2}\rho SpD^2C_{mag-m}v\alpha - \frac{1}{2}\rho SDC_{M\alpha}v^2\beta + \frac{1}{2}\rho SD^2C_{Mq}vr\right) \tag{12}$$

As is exposed in the early work of [16], the complex reaction of the shell to aerodynamic forces and moment has a much simplified form when its axis of symmetry, its axis of rotation and the direction of motion of its center of mass though the air all coincide. This is precisely the case for the shells studied in the thesis. Actually, more advanced calculus, and several steps of careful first-order approximations [7], see [24, Chapter 10], allow one to derive the equation governing the Pitching and Yawing motion of the rotationally symmetric projectiles.

Our choice of incidence angles α, β differ from [24]. Ours are attached to the body, which makes it easier to relate them to the measurement of both strapdown transverse accelerometers (these angles are oscillating at the spin rate frequency), whereas in [24] the angles correspond to the horizontal and vertical oscillating motion as could be observed from the ground. Note α_2 and β_2, the angles considered by [24]. The correspondence is given, under a small total angle of attack assumption by

$$\begin{cases} \alpha_2 = \sin(pt)\,\alpha - \cos(pt)\,\beta \\ \beta_2 = -\cos(pt)\,\alpha - \sin(pt)\,\beta \end{cases} \tag{13}$$

By introducing the *complex yaw*

$$\xi = \alpha_2 + i\beta_2$$

one obtains the following complex valued ordinary differential equation

$$\ddot{\xi} + \frac{v}{D}(H - iP)\dot{\xi} - \frac{v^2}{D^2}(M + iPT)\xi = -iPG \tag{14}$$

with

$$H = C^*_{L\alpha} - C^*_D - \frac{MD^2}{I_t}(C^*_{Mq} + C^*_{M\alpha}), \quad P = \frac{I_l}{I_t}\frac{pD}{v}$$

$$M = \frac{MD^2}{I_t}C^*_{M\alpha}, \quad T = C^*_{L\alpha} + \frac{MD^2}{I_l}C^*_{mag-m}, \quad G = \frac{gD\cos\Phi}{v^2}$$

[7] during the whole flight (typically lasting less than 45 s for ballistic flight and less than 2 s for flat-fire) the spin rate remains very high, and the angles of attitude w.r.t. the wind frame remain small. Therefore, it is possible to study the attitude dynamics, and, in turn, the translational dynamics, under the assumption of small-angles.

where for each aerodynamic coefficient C_X one uses the scaled proxy

$$C_X^* = \frac{\rho S D}{2M} C_X$$

The complex equation (14) will be central in the works presented in the thesis. It has been established by several authors, under various forms, which are all equivalent: [17, 18, 25, 15], among others. Also, it has been shown to be a very good approximation to the actual flight of symmetric projectiles.

This equation is a linear, second order differential equation with "almost constant" (slowly-varying) complex coefficients. Assuming now that the coefficients are indeed constants (as a short-term approximation), solving (14) reveals that the pitching and yawing motion of a symmetric projectile consists of two modes that rotate at different frequencies so that the complex yaw ξ follows an *epicyclic motion* in the complex plane, i.e. a motion of the general form[8]

$$\xi(t) = A_n e^{i\omega_n t} + A_p e^{i\omega_p t} + A_0 \tag{15}$$

where ω_n and $\omega_p << \omega_n$ designate the so-called "nutation" and "precession" angular frequencies, respectively. The epicyclic motion is pictured in Figure 5.

The nutation and precession frequencies have symmetrical expressions

$$\omega_n = p\frac{I_l}{2I_t} + \frac{v}{2}(P_1^2 + P_2^2)^{\frac{1}{4}} \cos\left[\frac{1}{2}\arctan\left(\frac{P_2}{P_1}\right)\right] \tag{16}$$

$$\omega_p = p\frac{I_l}{2I_t} - \frac{v}{2}(P_1^2 + P_2^2)^{\frac{1}{4}} \cos\left[\frac{1}{2}\arctan\left(\frac{P_2}{P_1}\right)\right] \tag{17}$$

where analytic expression of P_1, P_2 in terms of the aerodynamics parameters of the shell and the variables (v, h, p) are given in [12]. The "body-attached" incidence angles are given by

$$\alpha + i\beta = -i\left(A_n e^{i(p-\omega_n)t} + A_p e^{i(p-\omega_p)t} + A_0 e^{ipt}\right)$$

FREQUENCY CONTENT OF THE 3-AXIS ACCELEROMETER SIGNALS

The angular frequencies appearing in the last equation are observed in the aerodynamics forces, and therefore, in the 3-axis accelerometer signals.

Figure 6 reports the theoretical values of the angular frequencies at stake over the course of a typical ballistic flight. This plots were obtained using the analytic expressions of the frequencies and a detailed aerodynamic model. As appears in eqs. (16) and (17), the frequencies of the epicyclic motion carry information on the velocity v. This property is instrumental in the study conducted in this article.

[8]This expression is only a short-term approximate solution.

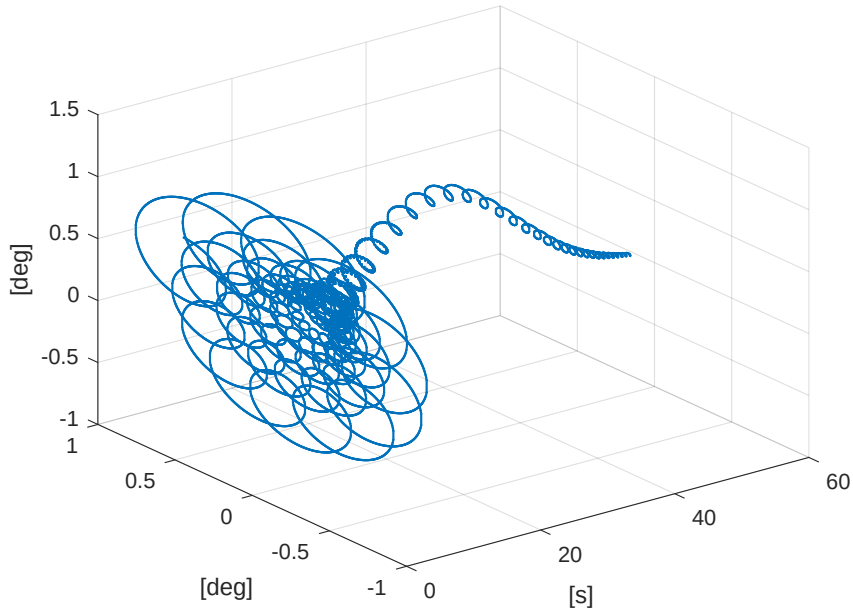

Figure 5: Epicyclic motion of the shell during a typical flight ; locus of the complex yaw ξ from Equation (15) [simulation results].

ONBOARD SENSORS

The strapdown sensors embedded into the shells (see Figure 7) consists of a 3-axis accelerometer and a 3-axis magnetometer. The data from the sensors is collected and sent by the radio frequency transmitter using the cone of the shell as a monopole antenna during the flight. The bandwidth allows to stream 2 megabytes of data per second with a low level of data losses[9]. All sensors are synchronous and sampled at the same rate (8064 Hz). The embedded systems is pictured in Figure 7.

Below, we describe several detrimental effects impacting the sensors and present mitigation means.

EDDY CURRENTS

Once embedded into the shell, the 3-axis magnetometer is heavily corrupted by an induction effect created by the high spin rate of the electrically conductive

[9] as will be visible when treating data, some outliers appears, especially at the end of the flight when the shell is the farthest from the receiving antenna.

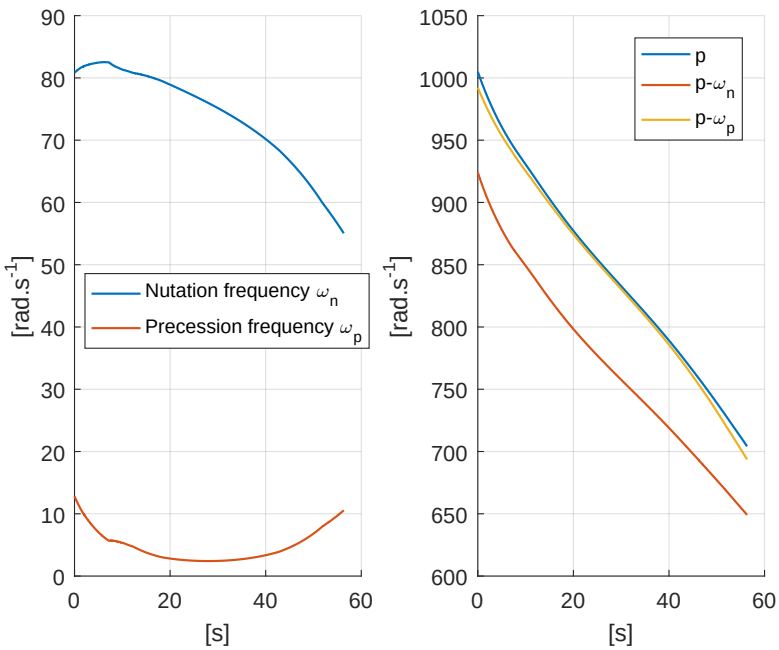

Figure 6: Theoretical frequencies of the epicyclic motion $\omega_p < \omega_n$ (left) and theoretical frequencies $p - \omega_n < p - \omega_p < p$ contained in the signal from any of the transverse accelerometers (right) [simulation data].

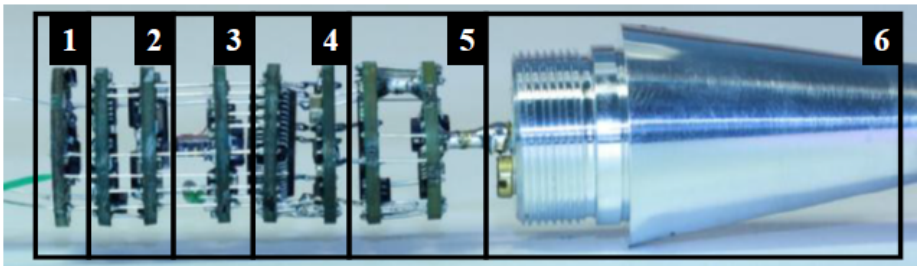

Figure 7: Embedded Instrumentation, from [6], used for the experiments studied in this article. 1: Power supply unit, 2: 3-axis magnetometer, 3: 3-axis accelerometer, 4: CPU (for signal conditioning), 5: RF Transmitter, 6: Monopole Antenna.

shell. This rotation around its main axis is the root cause for eddy currents. Fortunately, these effects can be mitigated by suppressing the known induction response to a given spin rate, previously modeled and measured on a testbed [6]. Using this compensation, it can be assumed that the induction effects are negligible. Accurate compensation requires to know the spin rate, the estimation of which is explained in Section .

MISALIGNMENT

Ideally, the sensors should be perfectly aligned with the body frame. In practice, there exists a small rotation between the sensors frame and the body frame, which results in a malicious modulation visible in the signals. In theory, there should be no oscillations at the spin rate frequency on the longitudinal magnetometer, but it is clearly seen in raw measurements. This fact suggests a procedure to address the misalignment. Simply, an additional rotation is applied to the measurements which minimizes the variance of the longitudinal component. The benefits of the misalignment compensation, and the reduction of the variance of the signal are illustrated in Figure 8.

FICTITIOUS FORCES

The accelerometers are disturbed by fictitious forces. Indeed, due to the high values of the spin rate under consideration (above 900 rad/s), even small residual misalignments (see §) or lateral shift of the sensors from the shell main axis induce substantial fictitious forces which directly corrupt the readings of the 3-axis accelerometer. Sensors are located in the nose of the shell, approx. 20 cm away from the center of mass of the shell. Interestingly, this is harmless for the frequency-based methodology. For reasons detailed below, the dominant fictitious forces share the same frequency content as the useful signals.

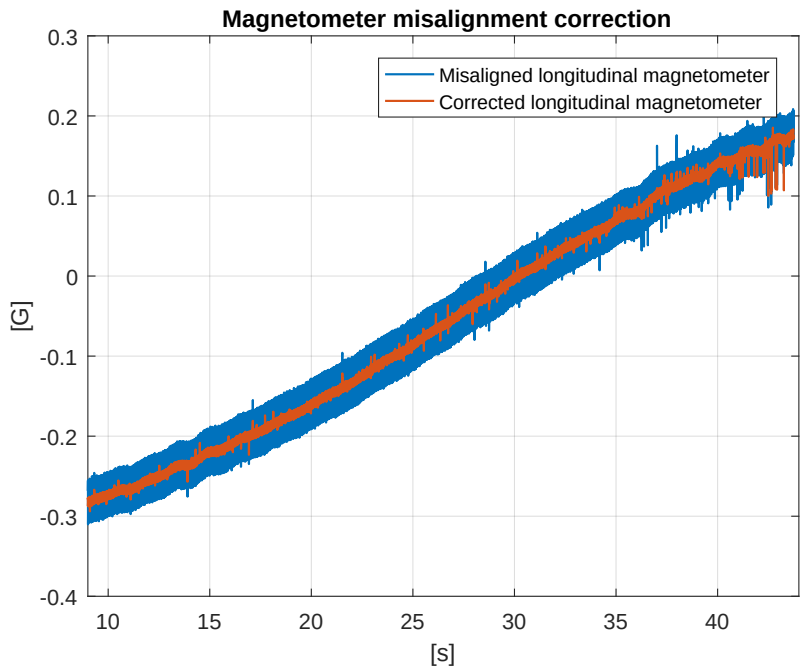

Figure 8: Compensation of the longitudinal magnetometer misalignment. A rotation of approximately 4 deg was employed. [experimental data].

In details, let Y_{acc0} denote the proper acceleration measured at the center of mass of the shell, then the proper acceleration occurring at a location shifted by a vector d is

$$Y_{acc} = Y_{acc0} + \Omega \times (\Omega \times d) + \frac{d\Omega}{dt} \times d \tag{18}$$

The longitudinal component of d is large. Furthermore, despite significant efforts in the mechanical design and construction phases, the sensors are not located right onto the shell symmetry axis, which correspond to small but non negligible *transverse* components in d. The high spin rate has a tremendous effect in (18) even for small such transverse shift. This effect is clearly visible in Figure 9 which compares experimental signals and their theoretical counterparts. According to (18), the factors that can cause fictitious forces are, and their orders of magnitude: Long. shift $d_1 = 10^{-1}$, Trans. shift $d_2 = 10^{-4}$, $d_3 = 10^{-4}$ (m), $p = 10^3$, $q = 10^1$, $r = 10^1$ (rad.s^{-1}). In turn, the various disturbance terms appearing in (18) are listed by descending order of magnitude in Table VIII. The "frequency content" column in Table VIII describes the oscillating contribution of each term (q and r obeying (11) and (12), respectively, and p being almost linearly damped according to (10)). It is worth mentioning that the term $d_1\,(p\,q + \frac{d}{dt}r)$ is actually much smaller than its constituting factors because, as can be seen in the last part of the rotational dynamics (12), one has that $I_t >> I_l$ implies

that $\frac{d}{dt}r \approx -p\,q$. This term is not negligible but it has the same frequency content as Y_{acc0}. Then, it appears that the dominant fictitious force is $-d_2\,p^2$ and that it acts as a (slowly drifting) bias on the 3-axis accelerometer. This drifting bias is visible in Figure 9 (bottom-left and -right plots). Interestingly, the bias is very large but it does not alter the frequency content of the 3-axis accelerometer signals.

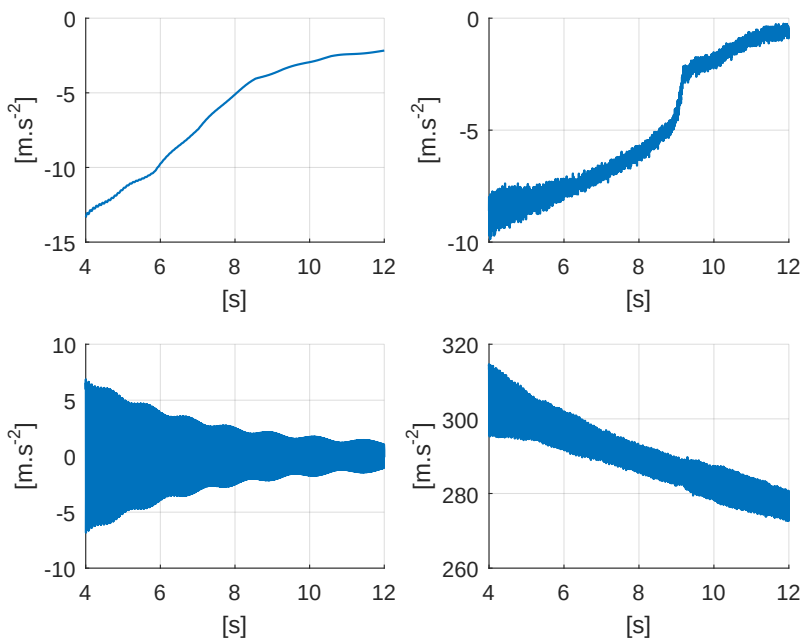

Figure 9: Values of longitudinal and transverse 3-axis accelerometer signals: simulation (left), experimental (right).

Table VIII: Signal at the center of mass and fictitious forces in one transverse accelerometer. Values in m.s^{-2}.

Expression	Range of value	Frequency content
Y_{acc0}	$10^1 \rightarrow 10^0$	$p, p-\omega_n, p-\omega_p$
$-d_2\,p^2$	10^2	None
$d_1(\,p\,q + \frac{d}{dt}r)$	$10^1 \rightarrow 10^0$	p, $p-\omega_n$, $p-\omega_p$
$d_3\,q\,r$	10^{-2}	Interference[10] of p, $p-\omega_n$, $p-\omega_p$
$-d_2\,r^2$	10^{-2}	Interference of p, $p-\omega_n$, $p-\omega_p$
$-d_3\,\frac{d}{dt}p$	10^{-3}	None

FREQUENCY-BASED ESTIMATION OF THE TRANSLATIONAL VELOCITY

ESTIMATION OF THE SPIN RATE

As seen in (10), the spin rate p has a practically autonomous dynamics with almost linear damping. Various methods can be employed to estimate the (vector) angular velocity without rate gyro, e.g. [13, 9, 22, 29, 23, 3]). Here, a simpler approach (complex argument method) can be used because the angular velocity (p, q, r) is actually close to (p,0,0). To estimate p, we apply the complex argument method presented in Appendix. Further, to filter any outliers, an extended Kalman filter with a model $\ddot{p} = 0$ is employed. Figure 10 reports estimates obtained from experimental signals.

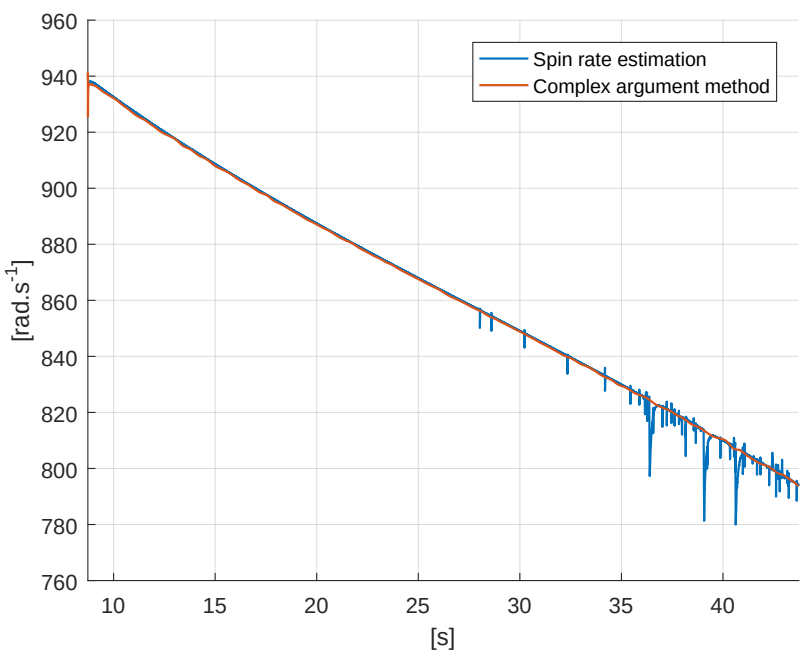

Figure 10: Estimation of spin rate [experimental results].

FREQUENCY DETECTION METHOD

From the expressions in eqs. (16) and (17), several frequencies can be used as sources to estimate the velocity from can be explored. We will choose to focus on $\omega_n >> \omega_p$ for two reasons. It is easier to measure on short time

windows (because a larger number of its periods can be observed over a given time window) and easier to distinguish from the spin rate in the accelerometer signal (see Figure 6-right).

The sensor signals contains the frequency $p - \omega_n$, while our interest lies in detecting ω_n. A solution is to treat the signal directly, detect $p - \omega_n$ as one of the frequencies of the signal, and deduce ω_n by substracting the known value of p (see §). This is possible, but is not the best option because, as illustrated in Figure 6, the frequencies peaks $p - \omega_n < p - \omega_p < p$ of the signal are relatively close, and the accuracy of the obtained estimate can be poor.

Several methods have been tested for frequency detection in this particular context, see [12]. Although all produce good results on simulation data, when employed on experimental data they are clearly outperformed by the *subspace* methods. They rely on the spectral decomposition of the autocorrelation matrix. Historically, the first subspace method was introduced by Pisarenko [26] and is now seen as a particular case of the MUSIC method introduced by Schmidt [28]. More details on the subspace method we used and the others we tested for comparison are given in [14].

APPLICATION TO THE TRANSVERSE ACCELEROMETER SIGNAL

The vectorspace algorithm we settled for is implemented to treat the transverse accelerometer signal. Analysis of the successive maxima of the frequency discriminating function gives the value of $p - \omega_n$. Once combined with the estimation of p from § , this gives an estimate of ω_n.

Signals measured during the flight suffer from a decreasing Signal-to-Noise Ratio (SNR) during the flight, consistently with the observed decay of the epicyclic motion pictured in Figure 5. We report the SNR of the 1-axis transverse accelerometer, as estimated from filtering, in Figure 11a. Also, data is also more corrupted when the shell gets further away from the receiving antenna, at the end of the flight. A time window $[8.75,\ 43.5]$ is selected. On average over the window, 4.6% of points in the dataset are corrupted. The obtained frequency estimate is of good quality at the beginning of the sequence and gets more noisy at the later stages, see Figure 11b. They are fitted to a fourth order polynomial in the time variable. The estimate is debiased so that it matches the model predictions at the end of the window.

REFERENCE VELOCITY

For reference, we use the velocity w.r.t. the local frame which is measured, on the shooting range with a ground-based position radar. The instant when the shell reaches Mach 1 is easily detected on the longitudinal accelerometer, under the form of a sudden jump of the signal. Comparing the value of 317 8 m/s

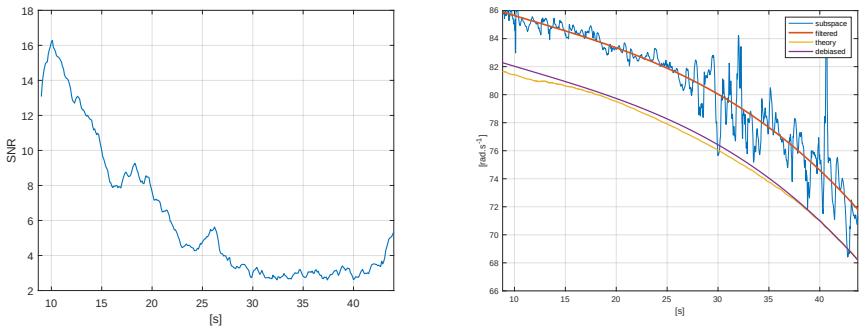

(a) Signal/noise ratio. $10 \cdot \log_{10}$ SNR is reported.

(b) Frequency detection against theoretical frequencies.

Figure 11: Experiments on frequency detection.

obtained from the frequency estimate through the velocity model with Mach 1 (332 m/s) [11], we deduce that our velocity estimate is biased (at this particular instant) by $\approx 13\,2$ m/s. Applying the inverse of the velocity model, we deduce our frequency estimate is biased by ≈ 2 Hz, and decide to apply a constant bias correction over the whole time interval. The result of this bias correction is reported in Figure 11b.

DESIGN OF AN OBSERVER FOR THE VELOCITY FROM FREQUENCY MEASUREMENTS

To estimate the translational velocity, a simple state observer can be used. It uses the open-loop dynamics of the translation velocity, which includes h and θ dependent terms that can be replaced with reference histories provided that they are well synchronized, which is easily done by detecting gun fire from any of the embedded signal, e.g. any of the accelerometers. The dynamics rewrite as a single-state time-varying nonlinear dynamics, with a nonlinear measurement equation (stemming from (16))

$$\frac{d}{dt}v(t) \triangleq f(v,t), \quad y(t) \triangleq g(v,t) \tag{19}$$

Observer design for this nonlinear dynamics (19) seems, at first, a routine problem. The main difficulty here is that g in (19) is not one-to-one. The behavior of aerodynamic drag-induced effects near Mach 1.0 implies that for any given t, the mapping $v \mapsto \frac{\partial g}{\partial v}(v,t)$ has a fixed number N of zeros (at least 2). They represent time-varying critical velocities. Although f becomes steep near these

[11] assuming the altitude is equal to the reference altitude for such a 155 mm fired at nominal speed, which is corroborated by the ground-based position radar measurements for sake of completeness.

points, it remains monotonic w.r.t. v at all times. Some analytical study reveals that $\frac{\partial C_D}{\partial v}$ remains small enough, for all v and t of interest in this study, so that $\frac{\partial f}{\partial v}$ stays strictly negative and bounded [12]. Therefore, the mapping f is a contraction in the sense of [19] and an observer is quite easy to design. To speed-up the convergence, we make an active usage of the measurement y using a gain having the same sign as $\frac{\partial g}{\partial v}$. Following common practice, see e.g. [4, 2, 7] and references therein, near the critical velocities, the gain is set to zero. This defines a gain-switching observer where the gain is a function of the current estimate. Exponential convergence analysis is given in [12]. The obtained results are reported in Figure 12.

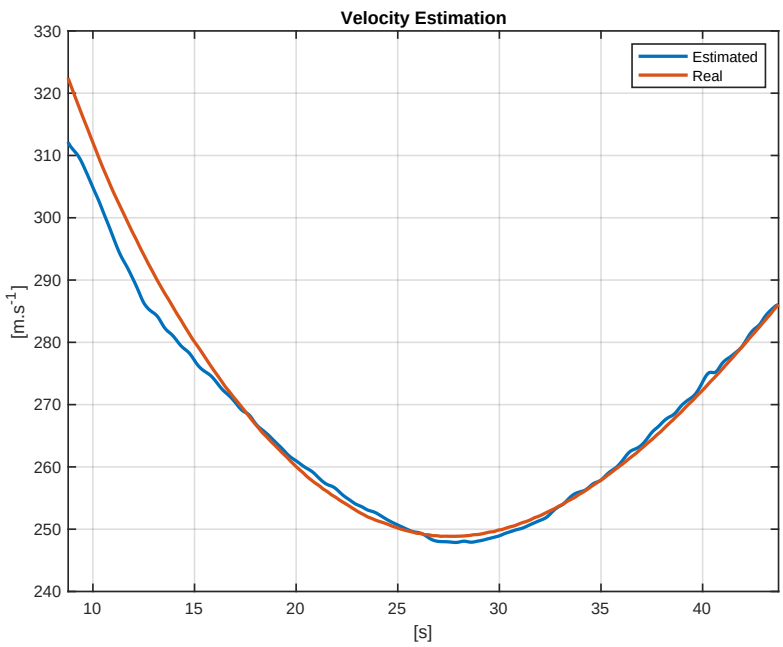

Figure 12: Velocity.

Figure 13: Velocity estimation [experimental results].

CONCLUSION AND ASSOCIATED WORKS

We have offered an efficient method to estimate the velocity of an artillery shell in free-flight, using only 3-axis magnetometer and 3-axis accelerometer (one axis was used only). Experimental results have been presented, and comparisons with high-fidelity measurements from a ground based position radar were

provided. These results stress the feasibility of the method, which uses a minimal set of sensors and induces a computational burden that is compatible with the specifications of standard embedded processors.

Two main possible follow-ups to the presented work are described next. First, the velocity estimation obtained without any ground-based position radar offers novel ways to calibrate shells' aerodynamic models simply by performing shots on the shooting range and treating on-board data. Second, the in-flight velocity estimation is a valuable intermediate variable to estimate the the projectile's position in a GNSS-denied environment. Even if the accuracy of the position will not be as good as with a GNSS receiver, it could be sufficient to make the projectile navigate to the basket where the seeker-head will detect the target.

Another natural follow-up is to use these results to improve the estimation of the projectile's attitude and position [11][27][8]

*

Outline of an attitude estimation method

As explained earlier, classic attitude estimation methods can not work as-is on-board a smart shell. We will not use any rate gyro, but when needed, an estimate of the angular velocity will be developed (this estimation will be referred to as a "virtual gyro"). The 3-axis magnetometer will be used as a body-frame measurement of the Earth magnetic field, whose coordinates b_0 in the local frame are known Besides, an additional input will compensate for the missing direction measurement usually given by the 3-axis accelerometer. The attitude will be represented under the form of a rotation matrix $\hat{R}$. A pictorial view of the estimation method is given in Figure 14.

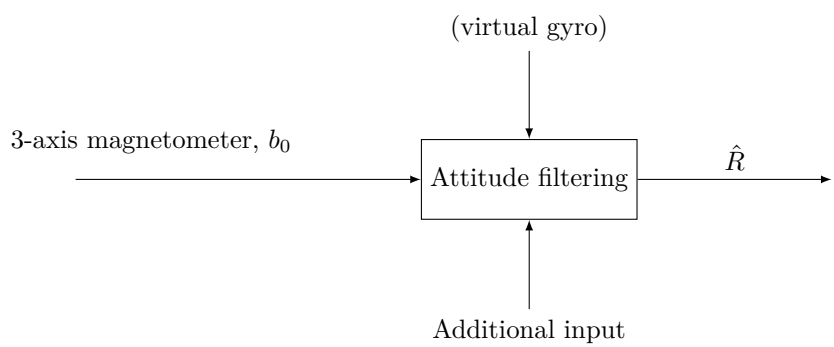

Figure 14: Attitude Filtering proposed in the thesis.

The "virtual gyro" can be a simple estimation of the dominant roll rate, which will be shown to be easily determined using the large oscillations observed

in both transverse accelerometers and transverse magnetometers signals[12].

The norm of the velocity w.r.t. the air can be obtained through a frequency analysis of the pitching and yawing motion induced by the aerodynamic moments. This estimation uses one of the transverse accelerometer as pictured in Figure 15.

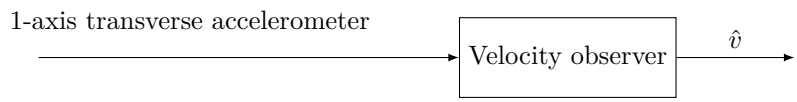

Figure 15: Velocity Estimation.

To compensate for the missing direction, one attitude angle will be directly estimated. Measuring only one direction makes one able to compute the attitude, up to a rotation by an unknown angle around the single known direction. If an additional "well-chosen" attitude angle is available, then the attitude estimation has only two isolated solution, that can be discriminated easily. The angle under consideration is the pitch angle. It is obtained from the estimate of the velocity w.r.t. the air, as pictured in Figure 16, which gives an approximation of it under the form of the slope angle. The pitch angle serves as "additional input" for the attitude observer of Figure 14 as pictured in Figure 17.

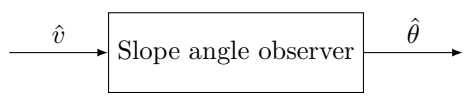

Figure 16: Slope angle Estimation.

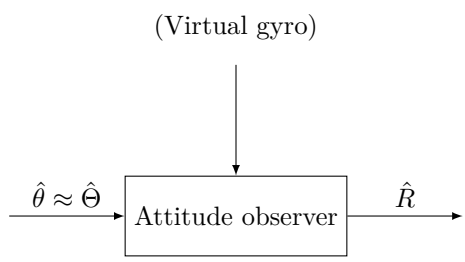

Figure 17: Attitude Estimation.

Finally, by connecting all the estimates described above, one obtains the overall attitude estimation methodology proposed in the thesis. It is described in Figure 18. It uses a 3-axis accelerometer (actually, only one of its transverse

[12] alternatively, one could use the knowledge of the aerodynamic moments, and the fact that 3-axis accelerometer provides a good estimation of the angular velocities through that modeling. Of course, using aerodynamic coefficients accordingly requires the knowledge of the velocity.

sensors) and a 3-axis magnetometer. Experimental results obtained with this method are given in [12].

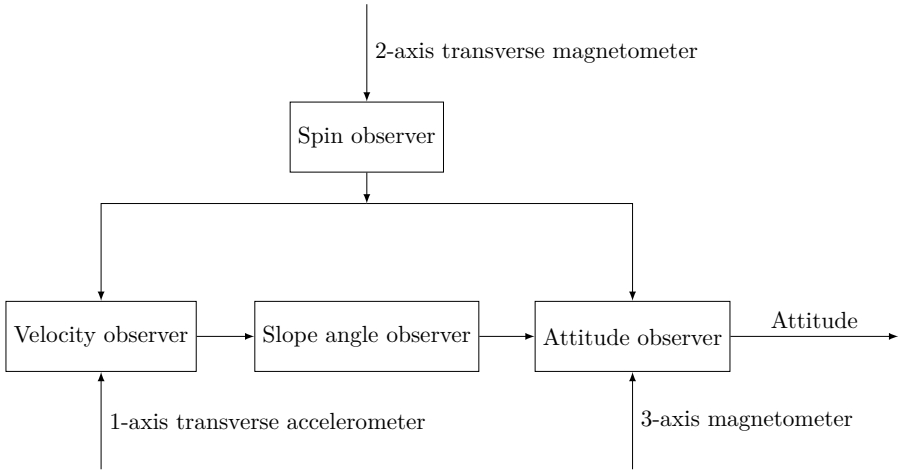

Figure 18: Attitude Estimation Algorithm from on-board sensors.

REFERENCES

[1] M. Albisser. *Identification of aerodynamic coefficients from free flight data.* PhD thesis, Université de Lorraine, 2015.

[2] A. Alessandri and P. Coletta. Switching observers for continuous-time and discrete-time linear systems. In *American Control Conference, 2001. Proceedings of the 2001*, volume 3, pages 2516–2521. IEEE, 2001.

[3] P. Cardou and J. Angeles. Estimating the angular velocity of a rigid body moving in the plane from tangential and centripetal acceleration measurements. *Multibody System Dynamics*, 19(4):383–406, 2008.

[4] D. Carnevale, D. Karagiannis, and A. Astolfi. Reduced-order observer design for systems with non-monotonic nonlinearities. In *Decision and Control, 2006 45th IEEE Conference on*, pages 5269–5274. IEEE, 2006.

[5] A. Carrière and L.-R. Oudin. Applications du calcul formel à la balistique. *Theoretical Computer Science*, 187(1):263 – 284, 1997.

[6] S. Changey, E. Pecheur, and P. Wey. Real time estimation of supersonic projectile roll angle using magnetometers: In-lab experimental validation. *IFAC Proceedings Volumes*, 42(5):123–127, 2009.

[7] A. A. Chunodkar and M. R. Akella. Switching angular velocity observer for rigid-body attitude stabilization and tracking control. *Journal of Guidance, Control, and Dynamics*, 37(3):869–878, 2014.

[8] C. Combettes, S. Changey, R. Adam, and E. Pecheur. Attitude and velocity estimation of a projectile using low cost magnetometers and accelerometers. In *2018 IEEE/ION Position, Location and Navigation Symposium (PLANS)*, pages 650–657. IEEE, 2018.

[9] M. Costello and T. Jitpraphai. Determining angular velocity and angular acceleration of projectiles using triaxial acceleration measurements. *Journal of spacecraft and rockets*, 39(1):73–80, 2002.

[10] A. D. Dupuis and W. Hathaway. Aeroballistic range tests of the basic finner reference projectile at supersonic velocities. Technical report, Defence Research Establishment Valcartier (Québec), 1997.

[11] L. D. Fairfax and F. E. Fresconi. Position estimation for projectiles using low-cost sensors and flight dynamics. *Journal of Aerospace Engineering*, 27(3):611–620, 2012.

[12] A. Fiot. *Attitude estimation of an artillery shell in free-flight from accelerometers and magnetometers*. PhD thesis, MINES ParisTech, PSL University, France, 2020.

[13] A. Fiot, S. Changey, C. Combettes, and N. Petit. A gyroless adaptation of attitude complementary filtering. In *Proc. of the European Control Conference (ECC)*, 2019.

[14] A. Fiot, S. Changey, and N. Petit. Attitude estimation for artillery shells using magnetometers and frequency detection of accelerometers. *Control Engineering Practice*, 122, 2022.

[15] V. Fleck. Introduction à la balistique extérieure avec exercices. *Cours de balistique extérieure, Coëtquidan*, 2005.

[16] R. H. Fowler, E. G. Gallop, C. N. H. Lock, and H. W. Richmond. The aerodynamics of a spinning shell. *Proceedings of the Royal Society of London. Series A, Containing Papers of a Mathematical and Physical Character*, 98(690):199–205, 1920.

[17] J. L. Kelley and E. J. McShane. On the motion of a projectile with small or slowly changing yaw. *Ballistics Research Laboratories Rep. No. 446, Dec. 1944*, 1944.

[18] R. H. Kent. Notes on a theory of spinning shell. Technical report, Ballistics Research Laboratories Rep. No. 898. 1954, 1954.

[19] N. N. Krasovskii. *Problems of the theory of Stability of Motion*. MIR, translated by Stanford University Press, 1963.

[20] L. Landau and E. Lifchitz. *Mechanics*. MIR Moscou, fourth edition, 1982.

[21] R. D. Lorenz. *Spinning Flight*. Springer, 2006.

[22] L. Magnis and N. Petit. Angular velocity nonlinear observer from single vector measurements. *Automatic Control, IEEE Transactions on*, 61(9):2473–2483, 2016.

[23] L. Magnis and N. Petit. Angular velocity nonlinear observer from vector measurements. *Automatica*, 75:46–53, 2017.

[24] R. L. McCoy. *Modern exterior ballistics*. Schiffer, 2nd edition, 1998.

[25] C. H. Murphy. Free flight motion of symmetric missiles. Technical report, Army Ballistic Research Lab Aberdeen Proving Ground MD, 1963.

[26] V. F. Pisarenko. The retrieval of harmonics from a covariance function. *Geophysical Journal International*, 33(3):347–366, 1973.

[27] J. Rogers, M. Costello, T. Harkins, and M. Hamaoui. Effective use of magnetometer feedback for smart projectile applications. *Navigation*, 58(3):203–219, 2011.

[28] R. Schmidt. Multiple emitter location and signal parameter estimation. *IEEE Transactions on Antennas and Propagation*, 34(3):276–280, March 1986.

[29] J. Shang, Z. Deng, M. Fu, and S. Wang. A high-spin rate measurement method for projectiles using a magnetoresistive sensor based on time-frequency domain analysis. *Sensors*, 16(6):894, 2016.

[30] P. Stoica and T. Soderstrom. Statistical analysis of MUSIC and subspace rotation estimates of sinusoidal frequencies. *IEEE Transactions on Signal Processing*, 39(8):1836–1847, August 1991.

[31] S. Weiss, K.-F. Doherr, and H. Schilling. Analytical solution and parameter estimation of projectile dynamics. *Journal of spacecraft and rockets*, 32(1):67–74, 1995.